A self-adaptive strategy for hybrid RANS/LES based on physical criteria

Martin David, Mahitosh Mehta, Remi Manceau

Highlights

A self-adaptive strategy for hybrid RANS/LES based on physical criteria

Martin David,Mahitosh Mehta,Rémi Manceau

- A self-adaptive strategy for hybrid RANS/LES is proposed.
- The mesh and the model are adapted based on physical criteria, with no intervention from the user.
- Resolved structures are rapidly generated in the LES region utilizing an active forcing.
- The approach is assessed on a flow over a backward facing-step.
- The method converges and the results are improved when compared to RANS k-ω SST.

A self-adaptive strategy for hybrid RANS/LES based on physical criteria

Martin David, Mahitosh Mehta and Rémi Manceau*

University of Pau & Pays Adour, E2S UPPA, CNRS, INRIA, CAGIRE project-team, Laboratory of Mathematics and Applied Mathematics (LMAP), Pau, 64000, France

ARTICLE INFO

Keywords:
Hybrid RANS/LES
Self-adaptive strategy
Physical criteria
Active forcing
Demonstrator

ABSTRACT

Hybrid RANS/LES methods can produce more reliable results than RANS with a reasonable computational cost. Thus, they have the potential to become the next workhorse in the industry. However, in continuous approaches, the location of the switching between the RANS and LES modes is based on the mesh generated by the user, such that the results are user-dependent. The present paper aims at developing a self-adaptive strategy, in which the RANS and LES zones are determined based on physical criteria, in order to mitigate the influence of the user. Starting from an initial RANS computation, successive HTLES are carried out and the mesh is refined according to the criteria, which are discussed at the beginning of the paper. In order to demonstrate the feasibility of this strategy, the method is applied to the case of a backward-facing step with the Hybrid Temporal Large Eddy Simulation (HTLES) approach, but is suitable for any other hybrid approach. The results obtained show that the method converges after only a few simulations and significantly improves the predictions when compared to RANS, with no intervention from the user. The power spectral density plots and Q-criterion visualization highlight the physical consistency of the results and the comparison of statistically averaged quantities with the DNS is very encouraging. Even though the process is still a long way from being applicable to a wide range of turbulent flows, this paper is a demonstrator of the applicability of this self-adaptive strategy.

1. Introduction

The Reynolds-Averaged Navier-Stokes (RANS) method makes it possible to investigate industrial cases due to its low computational cost, but often lacks reliability and only produces statistical results. On the other hand, LES, by only modeling the small turbulence scales, generally provides more accurate results and gives access to unsteady information. However, its computational cost remains too high in wall-bounded high Reynolds number industrial configurations. Even if the computing power is expected to continue increasing, Large Eddy Simulation (LES) should remain too expensive in many domains in a foreseeable future [22].

In most cases, it is desirable to resolve a larger range of the turbulence spectrum to get more information on the flow and handle strongly swirling flows, large-scale separation, acoustics sources, *etc*. Hybrid RANS/LES models are thus very promising since they can drastically reduce the computational cost of LES, give access to time-dependent information, and provide more reliable results than RANS. In these approaches, modeled motions, associated with the RANS and the LES models, and resolved motions, associated with the unsteady modes captured in the LES region, coexist. Hybrid RANS/LES methods may be divided into two categories: zonal, or discontinuous, and non-zonal, or continuous, approaches. In the first case, two different models are used in two subdomains. The main challenge with these approaches is to deal with the boundary conditions at the interface between the two modes. In non-zonal, or continuous approaches, only one set of equations is used and the transition from RANS to LES relies on model parameters updated during the computation, which makes them more flexible and is the reason for growing interest. Some of the most usual non-zonal hybrid RANS/LES approaches are the family of Detached Eddy Simulation (DES) models [24], the Partially-Integrated Transport Model (PITM) [5], the Partially-Averaged Navier-Stokes (PANS) method [11], and the Scale-Adaptive Simulation (SAS) [17]. The reader is referred to Chaouat [4] or [12] for recent reviews of hybrid RANS/LES methods.

In most hybrid RANS/LES approaches, the model is explicitly mesh size-dependent, making the position of the RANS and LES zones highly dependent on the mesh design chosen by the user. Based on his intuition and/or experience of the flow under consideration, and his knowledge of the limitations of RANS models, the user will choose to refine the mesh where he feels it is necessary to switch to LES mode. This is illustrated by Fig. 1 for the example of a backstep flow: two users may generate very different meshes, yielding different LES regions and, consequently, different results. Such user influence is highly dangerous in an industrial context, and in order to ensure the reliability of CFD for the design, dimensioning, and certification of industrial systems [19, 25], mitigating the user influence is of major importance.

Some approaches, often referred to as *self-adaptive*, break the explicit link between model and local grid step. The switch from RANS to LES is then driven by a physical criterion evaluated during the computation, such as the ratio between

*Corresponding author

martin.david@inria.fr (M. David); remi.manceau@inria.fr (R. Manceau)

ORCID(s): 0000-0001-5213-8712 (M. David); 0009-0007-7305-5378 (M. Mehta); 0000-0002-3964-161X (R. Manceau)

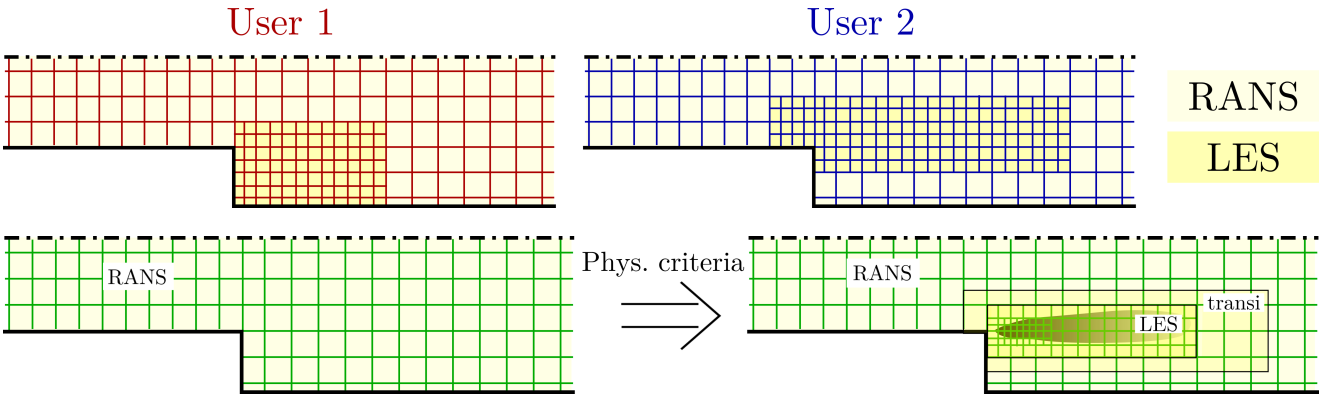

Figure 1: Schematic view of the problem (here non-conformal grid are represented for the sake of clarity). Top: Usual user-dependent hybrid RANS/LES. Bottom: Proposed self-adaptive strategy.

the integral and von Kármán length scales [17, 13] or the ratio of modeled to total turbulent energy [11, 20, 21, 2]. This type of models, called *second generation URANS* models by Fröhlich and von Terzi [9], introduces a partial decoupling between the model and the mesh, enabling the model, for example, to decide to remain in RANS mode even if the mesh is fine. The physical criteria used enable the model to detect whether turbulent structures appear locally in the resolved field, and to reduce the turbulent viscosity or the Reynolds stresses accordingly. However, it is clear that the decoupling is not complete, since the size of the resolved structures is still constrained by the grid, and the model cannot switch to LES mode if the mesh is too coarse, such that the user's influence remains very significant.

A way of avoiding the latter problem is that the mesh size is not set by the user, but by an adaptive meshing process. A few studies have explored hybrid RANS/LES methods focused on investigating mesh self-adaptivity within a predetermined and fixed LES region. Limare et al. [15], using DES, proposed remeshing based on physical criteria, to adapt the mesh in the LES zone using a simulation strategy combining an octree-AMR and overset grids. The grid size is partly controlled by one of the three following criteria, depending on the case study: the laminar-to-turbulent viscosity ratio, the von Kármán length scale-to-grid step ratio, or the Taylor length scale-to-grid step ratio. Assessing local LES-resolution sensors for hybrid RANS/LES simulations, Reuß et al. [23] performed Improved Delayed Detached-Eddy Simulation (IDDES) of a flow over a backward-facing step. They studied different formulations of a mesh sensor that detect under-resolved regions in LES region and can be used as input for automatic and local mesh refinement. Specifically, they proposed to refine the mesh in the LES region if the resolved turbulent kinetic energy is less than an arbitrary target of 80% of the total turbulent kinetic energy outside of the RANS region.

One step further is the work of Woodruff [27], in which the extent of the LES region is also self-adaptive. The location and size of the LES region are imposed by the user at the beginning of the workflow, then the region is allowed to grow until the solution becomes insensitive to this growth, and the grid size is adapted based on the local value of the strain rate. In this approach, the position of the LES zone is still determined by the user, based on his a priori knowledge of the flow, but the size of this zone and the mesh refinement are determined adaptively.

The aim of the present study is to develop a fully self-adaptive approach in which the user does not influence the definition of the RANS and LES regions and the resolution in the LES region. Starting from a RANS computation with a mesh obtained after a grid convergence study, the proposed method autonomously determines both the LES and RANS/LES transition regions, along with the size of the cells in the LES region based on physical criteria, as illustrated in Fig. 1. As RANS results are grid converged, they are considered here to be independent of the user. However, it is possible to rely on a RANS calculation with automatic mesh refinement, so as to completely avoid any user influence on the initial state of our algorithm. Successive hybrid RANS/LES computations are conducted and the characteristics of the LES and transition regions are updated after each simulation until convergence is achieved. As a demonstrator, the strategy is applied to the backward-facing step case [14] using the HTLES approach [7], in its active version [16].

The paper is organized as follows: our self-adaptive strategy is described in section 2, focusing on the possible physical criteria to identify the region where LES is necessary (section 2.1), the way to determine the size a RANS/LES transition region (section 2.2), and criteria used to fix the targeted grid step in the LES region (section 2.3). The hybrid RANS/LES model used for testing this strategy, the active HTLES of Mehta et al. [16] is described in section 3. Finally, in section 4, the self-adaptive strategy is evaluated in the case of a backward-facing step, by investigating the evolution of the RANS and LES zones and the associated mesh during successive iterations of the algorithm, as well as comparing of the results with Direct Numerical Simulation (DNS) data.

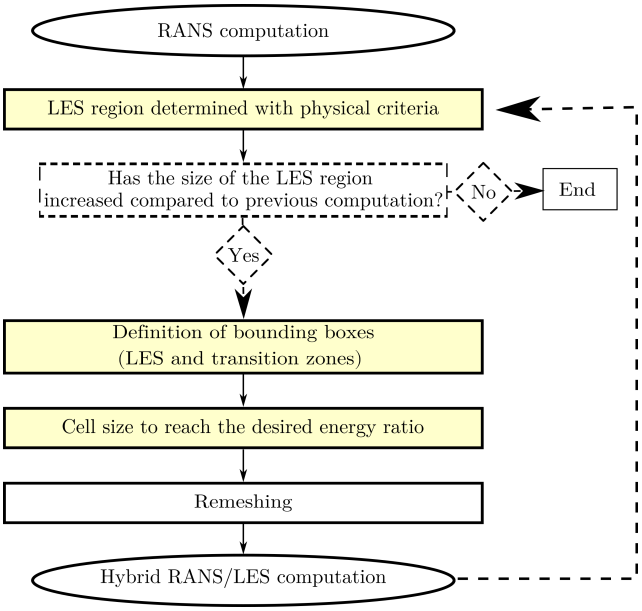

Figure 2: Algorithm used for the self-adaptive approach.

2. Self-adaptive strategy for hybrid RANS/LES

The proposed self-adaptive strategy is summarized in Fig. 2. This method aims at autonomously determining the LES and transition zones as well as the cell size in the LES zone. It consists in successive simulations to iteratively update the zones and the cell size until the convergence of the algorithm is reached. More precisely, the algorithm is initialized by a grid-converged RANS calculation. The RANS results are used to evaluate, based on a physical criterion, in which region to switch to LES mode. Two nested boxes are defined, delimiting the LES region and the RANS/LES transition region. The mesh in these two boxes is then refined to satisfy a resolution criterion. A new calculation is performed in hybrid RANS/LES using this automatically refined mesh. The physical criterion for determining the LES zone is updated on the basis of the average solution obtained in this hybrid RANS/LES simulation. If the LES zone is larger than previously, then a new iteration of the algorithm is performed. Otherwise, the algorithm stops and the solution obtained at this iteration is the result of the auto-adaptive process.

The three steps highlighted in yellow correspond to pivotal aspects of the present study and are detailed in subsections 2.1, 2.2, and 2.3.

2.1. Where to switch to LES?

The physical criteria used to define the refinement region in the framework of self-adaptive hybrid RANS/LES must be

(i) based on Reynolds-averaged quantities,
(ii) independent of the grid step,
(iii) non-dimensional,
(iv) objective (independent of the reference frame).

Based on these constraints, several physical criteria have been investigated from RANS results obtained in the case of a backward-facing step [14], with a bulk Reynolds number $Re = U_H H/\nu = 5000$, where H is the half-width of the channel and U_H the bulk velocity downstream of the expansion. The expansion ratio h/H is $2/3$. Only the lower half of the domain is considered with a symmetry applied at $y/H = 1$. The extent of the computational domain is $4H$ upstream and $16H$ downstream. In the spanwise direction, the domain size is H and the flow is periodic. A periodic RANS channel flow computation is used as the inlet boundary condition. The RANS model is the k-ω-SST model [18].

Note that in the present work, all the computations are carried out using code_saturne, a general CFD solver developed by EDF [1], based on a finite-volume method and a fully collocated arrangement for all the variables. A standard predictor-corrector scheme (SIMPLEC) is used to solve the velocity-pressure system. The Crank-Nicholson time scheme and a second-order (upwind in the RANS zone, centered in the LES zone) convection scheme are used. For hybrid RANS/LES, the statistical quantities are evaluated using both temporal averaging and spatial averaging in the periodic direction (z).

Numerous physical criteria corresponding to the constraints listed above have been considered and evaluated on the basis of RANS results. Those that seem most relevant, at least for the case of the backward-facing step, are presented in Fig. 3. They involve the turbulent kinetic energy, k, the production of turbulent kinetic energy, P, the dissipation, ϵ, the strain rate $\widetilde{S} = \sqrt{2S_{ij}S_{ij}}$, the Taylor length scale, $l_T = \sqrt{10\nu_t k/\epsilon}$, the Von Kármán length scale, $l_{VK} = K\widetilde{S}/|H|$, where $K = 0.41$ and $|H|$ is the Frœbenius norm of the Hessian matrix of the velocity. Overall, the criteria studied show a sharp increase downstream of the step, then the region colored in red extends downstream and moves away from the bottom wall. This is explained by the flow separation and the development of a reattached boundary layer. In Figs. 3a and 3b, the criteria exhibit high values in the detached shear layer, the near wall region, and the beginning of the recirculation zone. As the near-wall region is intended to stay in RANS mode, they are not adopted for this self-adaptive strategy. The third criterion presented (Fig. 3c) shows three thin red zones: the first follows the wall and is mainly due to the term $\epsilon/k^{3/2}$. The second and the third zones are induced by the first-order derivative-to-second-order derivative ratio involved in the Von Kármán length scale. This criterion, which is used in SAS to identify regions where turbulent structures appear in the resolved field, is therefore unsuitable for identifying detached shear layers from a Reynolds-averaged solution. The last two criteria quite satisfactorily identify the detached shear layer. For these reasons, any of the two first criteria could be used in the case of the backward-facing step. Combining different criteria to make the adaptive approach ready for a wide range of applications is beyond the scope of the present paper.

Therefore, in order to demonstrate the applicability of the adaptive strategy, the criterion chosen herein is simply

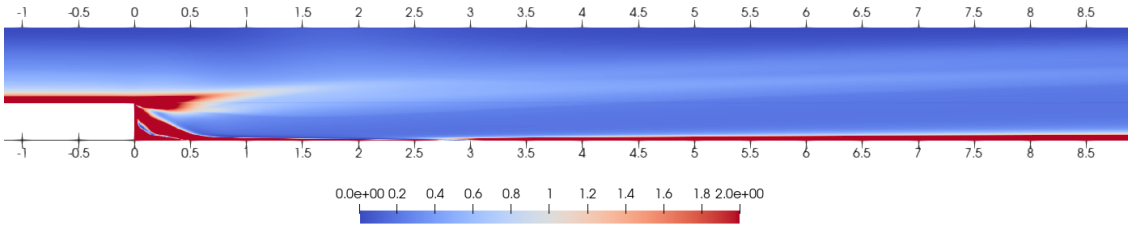

(a) $\frac{l_T^2 \widetilde{S}^2}{k}$

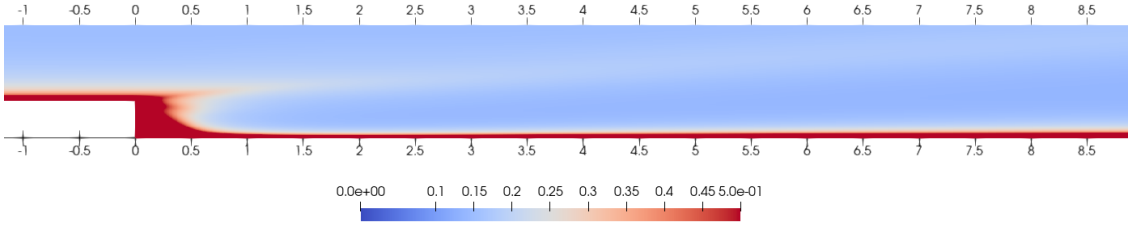

(b) $\frac{l_T \epsilon}{k^{3/2}}$

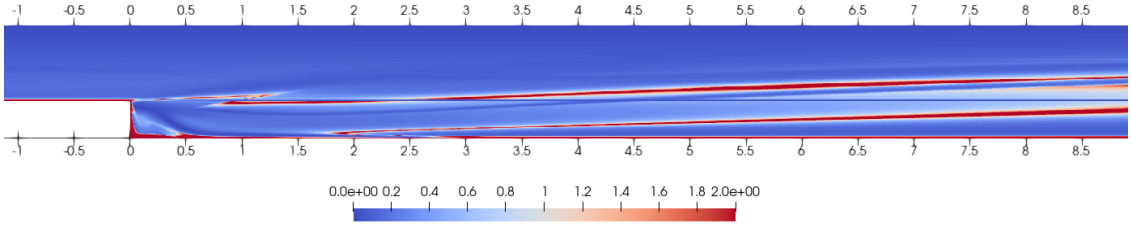

(c) $\frac{l_{VK} \epsilon}{k^{3/2}}$

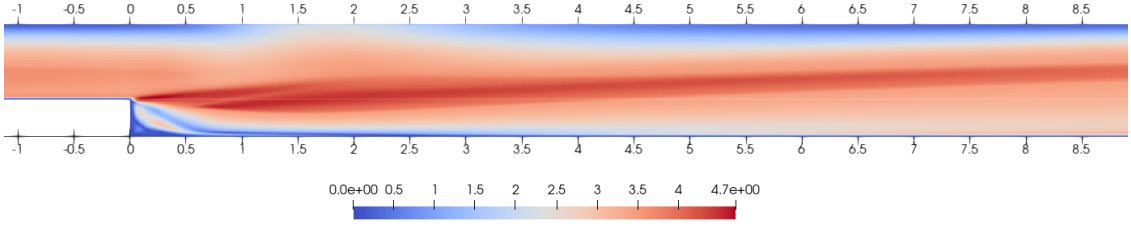

(d) $\frac{k\widetilde{S}}{\epsilon}$

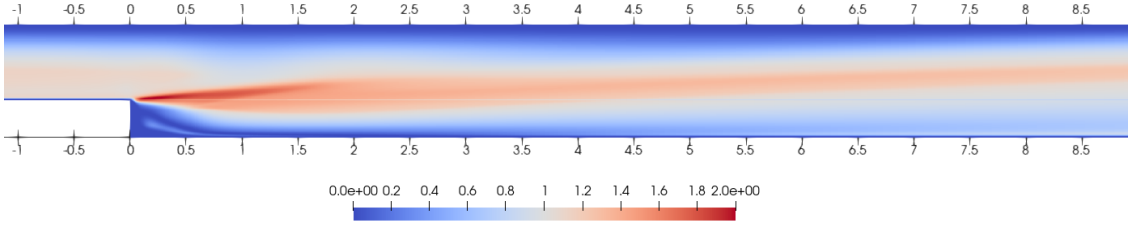

(e) $\frac{P}{\epsilon}$

Figure 3: Isocontours of some candidate physical criteria for defining the interface between RANS and LES.

the production-to-dissipation ratio. This criterion makes it possible to separate the zones close to equilibrium, where RANS models are generally sufficiently accurate, and the out-of-equilibrium zones where it is preferable to switch to LES mode to improve the quality of the results. Thus, regions where to switch to LES are identified via the threshold

$$\frac{P}{\epsilon} > \alpha, \tag{1}$$

where P and ϵ are the total production and total dissipation, respectively, and the threshold is chosen as $\alpha = 1.4$. Figure 4 shows the region identified by this criterion. The total

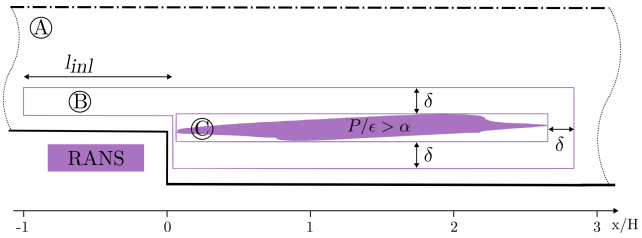

Figure 4: Visualization of the region where $P/\epsilon > \alpha$ based the RANS computation performed with the $k-\omega$ SST model. The two bounding boxes delimit zones A, B, and C corresponding to the RANS, RANS/LES transition, and LES zones, respectively.

production is obtained from

$$P = -\left(\overline{u_i' u_j'} + \tau_{ij}^{\mathrm{m}}\right) S_{ij}. \tag{2}$$

$\overline{u_i' u_j'}$ is the Reynolds-averaged (in practice, averaged in time and in span), which is zero in a RANS computation. τ_{ij}^{m} is the Reynolds-averaged sub-filter stress tensor, equal to the Reynolds-stress tensor in RANS mode, and S_{ij} is the mean strain rate tensor. The total dissipation is computed as

$$\epsilon = \epsilon_{\mathrm{m}}/r_\epsilon, \tag{3}$$

where ϵ_{m} is the Reynolds-averaged sub-filter dissipation. r_ϵ is the ratio of the modeled dissipation ϵ_{m} to the total dissipation ϵ, which is equal to one in RANS mode and also generally considered very close to one in LES mode, since the small scales are not resolved [7]. However, in low Reynolds number regions, such as the recirculation region downstream the backstep, a small part of the dissipation can be resolved. This must be accounted for in order not to bias the evaluation of the criterion (1). The determination of r_ϵ in the framework of the HTLES model used herein will be presented in section 3.

2.2. How to ensure the RANS/LES transition?

Bounding boxes are defined around the region satisfying the physical criterion given by Eq. (1) in order to adapt the mesh, as shown in Fig. 4. For practical reasons, the RANS, RANS/LES transition, and LES zones are denoted A, B, and C, respectively. They are obtained using the following rules:

(i) The LES zone (zone C) is the smallest rectangle containing the $P/\epsilon > \alpha$ region.

(ii) The transition zone (zone B) is used to smoothly link the meshes used in LES and RANS zones. It is characterized by a rectangular shape bounding the LES zone with a thickness $\delta = 0.5\,\langle l_I \rangle_{P/\epsilon>\alpha}$ where $\langle l_I \rangle_{P/\epsilon>\alpha}$ is the mean of the integral length scale in the zone satisfying Eq. (1). If at the end of a simulation the region corresponding to $P/\epsilon > \alpha$ extends until the bounds of the transition zone, the thickness δ of this zone is multiplied by 10 in this direction for the next iteration of the algorithm, to reduce the total number of iterations to reach the convergence of the adaptive method. Upstream, the beginning of the transition zone is fixed with a length of

$$l_{inl} = C_{inl}\delta, \tag{4}$$

where $C_{inl} = 5$ is a constant, which is determined by a preliminary study presented in Sec. 4.1. This is the minimal length required for the volume forcing presented in Sec. 3.2 for generating turbulent structures. Note that, since a shielding function is applied in the hybrid RANS/LES model until $y^+ = 20$ to enforce the RANS mode in the near wall region, this shielded region is excluded from zone B.

(iii) The RANS zone (zone A) is the rest of the domain. The RANS mode of the hybrid RANS/LES model is imposed. In this zone, the mesh will not be refined.

2.3. What is the targeted cell size in each region?

In order to provide a user-independent method, the mesh size in the LES region must now be set by an objective criterion. The criterion chosen here is the ratio r_K of modeled energy k_m to total turbulent energy k_r. Assuming a Kolmogorov spectrum, we have

$$r_K = \frac{k_{\mathrm{m}}}{k} = \frac{1}{k}\int_{\kappa_c}^{\infty} E(\kappa)\mathrm{d}\kappa = \frac{3C_\kappa}{2}\left(\kappa_c \frac{k^{3/2}}{\epsilon_m}\right)^{-2/3}, \tag{5}$$

with $\kappa_c = \pi/\Delta$ the cutoff wavenumber and $k = k_m + k_r$. The cell size to reach the targeted energy ratio r_K is thus computed as

$$\Delta = \pi\left(\frac{2}{3}\frac{r_K}{C_K}\right)^{3/2}\frac{k^{3/2}}{\epsilon_m}. \tag{6}$$

Since it is linked to the integral length scale $k^{3/2}/\epsilon_m$, Δ is variable in space and is given as a local target to the meshing tool.

The rules followed to build the new mesh are:

(i) In the RANS zone (zone A): the mesh is kept unchanged.

(ii) In the LES zone (zone C): the new unstructured mesh is built, composed of cells whose local target size is given by Eq (6).

(iii) In the transition zone (zone B): the targeted cell size in the transition zone is equal to the maximum cell size obtained in the LES zone and the smooth transition between the structured RANS and unstructured LES meshes is ensured by the meshing tool.

In this study, the GMSH software [10] is used to generate the grids. The unstructured zones are meshed with the Packing of Parallelograms algorithm.

3. Turbulence modeling

Although the self-adaptive methodology can be associated to any continuous hybrid RANS/LES approach, HTLES-$k-\omega$-SST [7] is used in the present study, in its active version recently proposed by Mehta et al. [16]. For more details, the reader is referred to these two papers.

3.1. Hybrid Temporal LES (HTLES)

Derived from the PITM model [5, 8], the HTLES is a continuous hybrid approach in which the hybridization term in the energy equation is based on a time scale driven by the energy ratio r. The equations resolved are the following:

$$\begin{cases} \nu_{\mathrm{sfs}} = \dfrac{a_1 k_{\mathrm{sfs}}}{\max\left[a_1\psi(r)\omega^*_{\mathrm{sfs}}, F_2\widetilde{S}\right]}, \\ \dfrac{\partial k_{\mathrm{sfs}}}{\partial t} + \widetilde{U}_k\dfrac{\partial k_{\mathrm{sfs}}}{\partial x_k} = P_{\mathrm{sfs}} + D_{k\mathrm{sfs}} - \dfrac{k_{\mathrm{sfs}}}{T_{\mathrm{m}}}, \\ \dfrac{\partial \omega^*_{\mathrm{sfs}}}{\partial t} + \widetilde{U}_k\dfrac{\partial \omega^*_{\mathrm{sfs}}}{\partial x_k} = \gamma_\omega\dfrac{\omega^*_{\mathrm{sfs}}}{k_{\mathrm{sfs}}} + D^*_{\omega\mathrm{sfs}} \\ \qquad\qquad -\beta_\omega {\omega^*_{\mathrm{sfs}}}^2 + C^*_{\omega\mathrm{sfs}}, \end{cases} \tag{7}$$

with the production limiter

$$P_{\mathrm{sfs}} = \min\left[\nu_{\mathrm{sfs}}\widetilde{S^2}, a_2 C_\mu k_{\mathrm{sfs}}\psi(r)\omega^*_{\mathrm{sfs}}\right], \tag{8}$$

the diffusion terms

$$D_{k\mathrm{sfs}} = \frac{\partial}{\partial x_j}\left[\left(\nu + \frac{\nu_{\mathrm{sfs}}}{\sigma_k}\right)\frac{\partial k^*_{\mathrm{sfs}}}{\partial x_j}\right] \tag{9}$$

and

$$D_{\omega\mathrm{sfs}} = \frac{\partial}{\partial x_j}\left[\left(\nu + \frac{\nu_{\mathrm{sfs}}}{\sigma_\omega}\right)\frac{\partial \omega^*_{\mathrm{sfs}}}{\partial x_j}\right], \tag{10}$$

and the cross-diffusion term,

$$C^*_{\omega\mathrm{sfs}} = (1-F_1)^2\frac{1}{\sigma_{\omega_2}}\frac{1}{\psi(r)\omega^*_{\mathrm{sfs}}}\frac{\partial \omega^*_{\mathrm{sfs}}}{\partial x_j}\frac{\partial k_{\mathrm{sfs}}}{\partial x_j}. \tag{11}$$

$\beta_\omega = C_\mu(C_{\epsilon 2} - 1)$, $\gamma_\omega = C_{\epsilon 1} - 1$, F_1 and F_2 the blending functions, and a_1, a_2, $C_{\epsilon 1}$, and $C_{\epsilon 2}$ are the usual coefficients of the k-ω SST model.

T_{m} is the turbulent time scale that drives the transition from the RANS mode to the LES mode

$$T_{\mathrm{m}} = \frac{r}{\psi(r)}\frac{k_{\mathrm{m}} + c_r k_r}{C_\mu k_{\mathrm{m}}\omega^*_{\mathrm{m}}}, \tag{12}$$

where c_r is the coefficient imposing the *internal consistency constraint*: in the RANS zone, resolved energy due to the penetration of turbulent structures from the LES region is not counted in the total turbulent energy in order to strictly tend to the RANS model in this zone,

$$c_r = \begin{cases} 0 \text{ if } r = 1, \\ f_s \text{ if } r < 1. \end{cases} \tag{13}$$

$\psi(r)$ is the hybridization function defined by

$$\psi(r) = \frac{\beta_\omega}{C_\mu\gamma_\omega + r(\beta_\omega - C_\mu\gamma_\omega)}. \tag{14}$$

This expression goes to unity when $r = 1$, such that the RANS model is recovered.

Table 1
Coefficients of the HTLES-$k-\omega$-SST model.

β_0	γ	C_1	C_2	p_1	p_2
0.48	2/3	13.5	1.2	8	6

The energy ratio

$$r = (1 - f_s) + f_s \times \min\left[1, r_K\right]. \tag{15}$$

involves the shielding function f_s introduced by Duffal et al. [7] to avoid grid-induced separation and the log-layer mismatch:

$$f_s = 1 - \tanh\left[\max\left(\xi_K^{p1}, \xi_D^{p2}\right)\right], \tag{16}$$

with $\xi_K = C_1\left(\nu^3/\epsilon\right)^{1/4}/d_w$, and $\xi_D = C_2\Delta_{max}/d_w$, where d_w is the distance to the wall and Δ_{max} the local cell elongation (longest edge of the cell). The energy ratio r_K, active far from the wall where the shielding function goes to one, is obtained analytically from an equilibrium Eulerian temporal spectrum [26],

$$r_K = \frac{1}{\beta_0}\left(\frac{U_s}{\sqrt{k}}\right)^{2/3}\left(\omega_c\frac{k}{\epsilon_m}\right)^{-2/3} \tag{17}$$

where

$$\epsilon_m = C_\mu k_{\mathrm{m}}\psi(r)\omega^*_{\mathrm{m}}, \tag{18}$$

$\omega_c = \min\left[\frac{\pi}{dt}, \frac{U_s\pi}{\Delta}\right]$ is the cutoff frequency, $\Delta = \Omega^{1/3}$ with Ω the cell volume, and $U_s = U + \gamma\sqrt{k}$ is the sweeping velocity. Note that in the present study, the time-step is smaller than Δ/U_s everywhere in the domain, such that $\omega_c = U_s\pi/\Delta$ and r_K is given by Eq. 5. The constants used are summarized in Tab. 1 and more details can be found in [7].

As mentioned in Sec. 2.1, the criterion $P/\epsilon > \alpha$ is biased if the resolved part of the dissipation is not taken into account, particularly in the low Reynolds number recirculation region. In order to avoid the cumbersome computation of the resolved part of dissipation during the simulation, Eq. (3) is used, where the modeled-to-total dissipation ratio r_ϵ is evaluated, assuming a Kolmogorov spectrum, from the definition of the energy and dissipation ratios, r and r_ϵ, respectively, and the integration of the energy and dissipation spectra between the integral and the Kolmogorov length scales. Denoting by a hat variables made non-dimensional based on ϵ, k and ν_t, we have

$$r_\epsilon = \frac{\hat{\epsilon}_{\mathrm{m}}}{\hat{\epsilon}} = \frac{1}{\hat{\epsilon}}\int_{\hat{\kappa}_c}^{\hat{\kappa}_\eta}\frac{2}{R_t}C_\kappa\hat{\kappa}^{1/3}\mathrm{d}\hat{\kappa}, \tag{19}$$

where $R_t = \nu_t/\nu$ is the turbulent Reynolds number, yielding

$$r_\epsilon = 1 - \frac{\pi^2}{\hat{\Delta}^{4/3}R_t}. \tag{20}$$

Similarly, from

$$r = \frac{\hat{k}_{\mathrm{m}}}{\hat{k}} = \frac{1}{\hat{k}} \int_{\hat{\kappa}_c}^{\hat{\kappa}_\eta} C_\kappa \hat{\kappa}^{-5/3} \mathrm{d}\hat{\kappa}, \tag{21}$$

one can obtain

$$r = \hat{\Delta}^{2/3} \frac{\pi^{2/3}}{R_t^{1/2}}. \tag{22}$$

Combining Eqs. (20) and (22) gives

$$r_\epsilon = 1 - \left(1 + \frac{r R_t^{1/2}}{\pi} \right)^{-2}. \tag{23}$$

Since dissipative scales are smaller than energetic scales, $r_\epsilon \geq r$, such that the final expression is

$$r_\epsilon = \max \left[1 - \left(1 + \frac{C_{r_\epsilon} r R_t^{1/2}}{\pi} \right)^{-2}, r \right]. \tag{24}$$

With this expression, $r_\epsilon = 1$ in the RANS mode since $r = 1$ and goes to zero at the DNS limit where $r = 0$. $C_{r_\epsilon} = 0.42$ is a coefficient calibrated by comparing dissipation fields obtained in hybrid RANS/LES and RANS.

3.2. Active approach

In continuous hybrid RANS/LES, during the transition from RANS mode to LES mode, the modeled turbulent energy is reduced by the model. However, the growth of the resolved energy is slow, leading to a strong local underestimation of the total turbulent energy and the turbulent stresses. To mitigate this gray area issue, Mehta et al. [16] have developed the *active* approach, which injects the proper amount of energy into the resolved motion via a body force in the momentum equation written as

$$f_i = A_{ij} \widetilde{U}_i + B_i, \tag{25}$$

where $\widetilde{U}_i$ is the resolved velocity. A_{ij} and B_i have to satisfy two constraints: (i) energy injection in the resolved scales is imposed by the rate of energy removal in the modeled scales; (ii) the forcing should not affect the mean flow. It can be shown that these constraint are satisfied if A_{ij} and B_i are determined by solving at each point of the domain the system

$$\begin{cases} A_{ik} \overline{u_j' u_k'} + A_{jk} \overline{u_j' u_k'} = -\tau_{ij}^{\mathrm{m}} \dfrac{1}{r} \dfrac{\mathrm{d}r}{\mathrm{d}t}, \\ B_i = -A_{ij} \overline{\widetilde{u}_j}, \end{cases} \tag{26}$$

where u_i' is the fluctuating part of the resolved velocity and $\overline{\cdot}$ stands for the Reynolds average. The force is thus a function of the rate of change of the energy ratio in the flow direction $\mathrm{d}r/\mathrm{d}t$ and goes to zero where the mesh is uniform. This *active* version of the HTLES is used for all the simulations in the present paper.

4. Results and discussion

4.1. Influence of the length of transition

The intensity of the fluctuating body force added to the momentum equation is determined by Eq. (26) and relies on the material derivative of the energy ratio r. Thus, increasing the length l_{inl} of the RANS-to-LES transition upstream the step corner (Fig. 4) has different and contradictory consequences. On the one hand, since the refinement of the mesh in the flow direction is less rapid, the energy ratio $r = k_m/k$ decreases more slowly and the intensity of the forcing is reduced. On the other hand, the resolved structures have more space for developing, since the force is active over a longer region. The influence of l_{inl} is in theory moderate, since these two effects compensate for each other: $(1/r) \times \mathrm{d}r/\mathrm{d}t \simeq (1/r) \times U \partial r/\partial x$ is of the order of U/l_{inl}, where U is the streamwise mean velocity, and since the distance travelled is l_{inl}, the work done by the force is globally independent of l_{inl}.

However, Mehta et al. [16] showed, in the case of a channel flow, that the realistic turbulent strucures cannot develop if the transition region is too short. Therefore, a preliminary study is performed here to determine the value of C_{inl} to be used in Eq. (4).

In this preliminary study, a structured mesh of 5.7M cells is used, which is fine enough to be in LES mode everywhere. However, the RANS mode is artificially imposed in the inlet channel, as well as a transition in the region $x \in [x_{\mathrm{trans}}; 0]$ upstream of the step. To achieve this, the energy ratio r related to the grid step given by Eqs. (15) and (17) is modified by imposing $r_{\mathrm{mod}} = 1$ in the inlet channel up to the position $x = x_{\mathrm{trans}}$ and then a gradual decrease of the form

$$r_{\mathrm{mod}} = f + (1 - f) r \quad \text{with} \quad f(x) = \frac{x}{x_{\mathrm{trans}}}, \tag{27}$$

such that the usual value of r is recovered at the step corner ($x = 0$). Two different cases are presented here, for $x_{\mathrm{trans}}/H = -1$ and $x_{\mathrm{trans}/H} = -2$, as shown in Fig. 5. For both cases, the resolved structures are rapidly developed, as soon as the energy ratio is lower than unity and the structures are advected downstream. The streamwise velocity profiles in Fig. 6 show that, for the two cases, the profiles are nearly superimposed, showing that $x_{\mathrm{trans}}/H = -1$ is sufficient. Reducing further the transition zone does not allow to generate realistic structures (not shown here). Since a slightly better agreement with DNS is found for the case with the shorter transition length, and with the purpose of reducing the global cost of the computations, this order of magnitude of $l_{inl}/H \approx 1$ is retained for building the zone B (see Fig. 4). Based on the RANS results, this approximately correspond to calibrating the constant in Eq. (4) as $C_{inl} = 5$.

4.2. Evolution of the zones and the mesh

The region where switching to LES mode is desirable obtained from Eq. (1), using $\alpha = 1.4$. The cell size to reach the targeted energy ratio r is given by Eq. (6). The targeted value $r = 0.1$ is used, except for the first iteration, called HTLES1 below, for which the less strict value $r = 0.15$ is

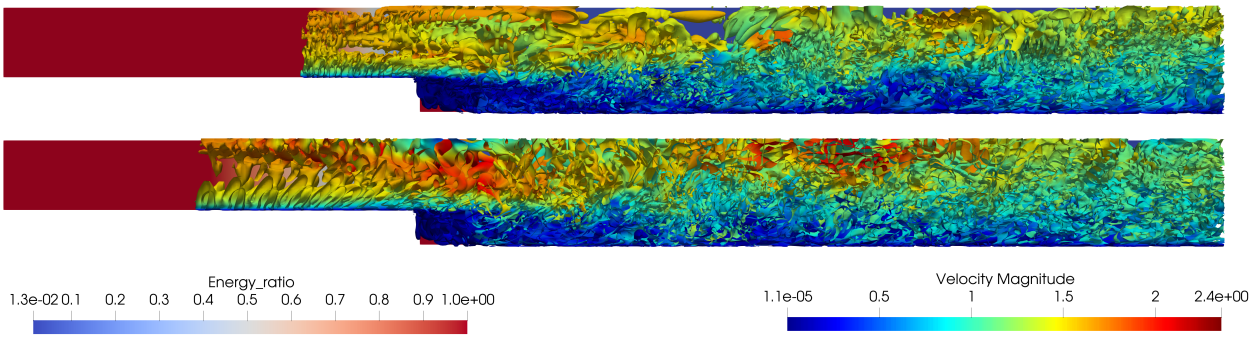

Figure 5: Q-isosurfaces colored by the velocity magnitude ($Q = 0.5U_H^2/H$) and targeted turbulent energy ratio.

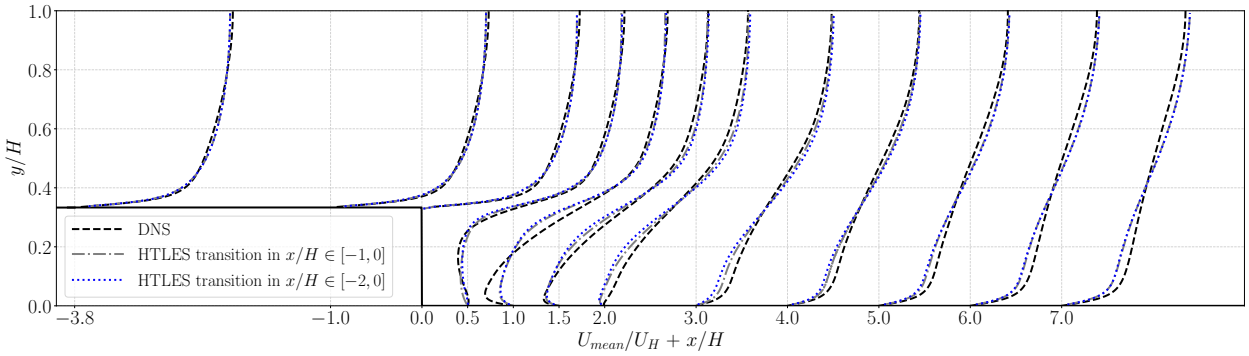

Figure 6: Streamwise velocity profiles in the y direction for 12 streamwise locations. DNS results are from Lamballais [14].

applied to save computational time, since it is only the first mesh determined by the probably inaccurate RANS results . The mesh and zone obtained for the successive computations are presented in Figs. 7 and 8.

A RANS computation, performed on a fully structured grid composed of 95 800 cells obtained after a grid convergence study, is used to initialize the algorithm. Note that the mesh consists of only one cell in the z direction due to spanwise periodicity. Following the rules presented in Sec. 2.2, the region corresponding to $P/\epsilon > \alpha$ is extracted and used to determine the boundaries of the LES and transition zones of the first HTLES computation (purple boxes). The cell size in the LES region is computed following the rules described in Sec. 2.3. The HTLES1 mesh is generated by GMSH according to these zones and cell size requirements. In the HTLES computations, the grids in the transition and LES zones are also refined in the z-direction to obtain cells which are as isotropic as possible. The HTLES1 computation is then performed and the region corresponding to $P/\epsilon > \alpha$ is updated based on the time-averaged results. Here, it extends until the end of the transition zone thus, following the rules established in Sec. 2.2, the thickness of the transition zone utilized for HTLES2 (largest red box at the bottom of Fig. 7) is increased in this direction to mitigate the total number of algorithm iterations. The same procedure is repeated for HTLES2 and HTLES3 (Fig. 8). The results of HTLES3 show that the area of the LES zone is reduced when compared to the one of HTLES2. This stops the algorithm, since the LES region is sufficiently large, and trying to optimize its size would lead to extra iterations of the algorithme that would actually increase the total computational cost. Here, we still performed a fourth HTLES run, using the same zones but cell sizes computed from HTLES3 results, to confirm the convergence of the results.

The cell number, the averaged value of Δ, the cell size to reach the targeted energy ratio in the region where the criterion (1) is satisfied and the area of zone C are shown in Fig. 9. Except for HTLES2 whose transition zone size has been increased, as explained above, to reduce the total number of algorithm iterations, the grid size exhibits a monotonic increase from RANS to HTLES4. The mesh obtained after the computation of HTLES4, which would have been used for HTLES5 if the algorithm were not stopped, is reduced when compared to the one obtained after HTLES3, highlighting the convergence of the method. After a monotonic increase, the value $\langle\Delta\rangle_{P/\epsilon>\alpha}$ obtained with HTLES3 is reduced when compared to HTLES2, and remains virtually constant between HTLES3 and HTLES4. A similar behavior is observed in the graph showing the evolution of the area of Zone C, with the stabilization of the LES zones. From these graphs, it is clear that the proposed method reaches convergence.

4.3. Comparison with DNS

In this section the results obtained after the different iterations of the algorithm are compared with DNS. The

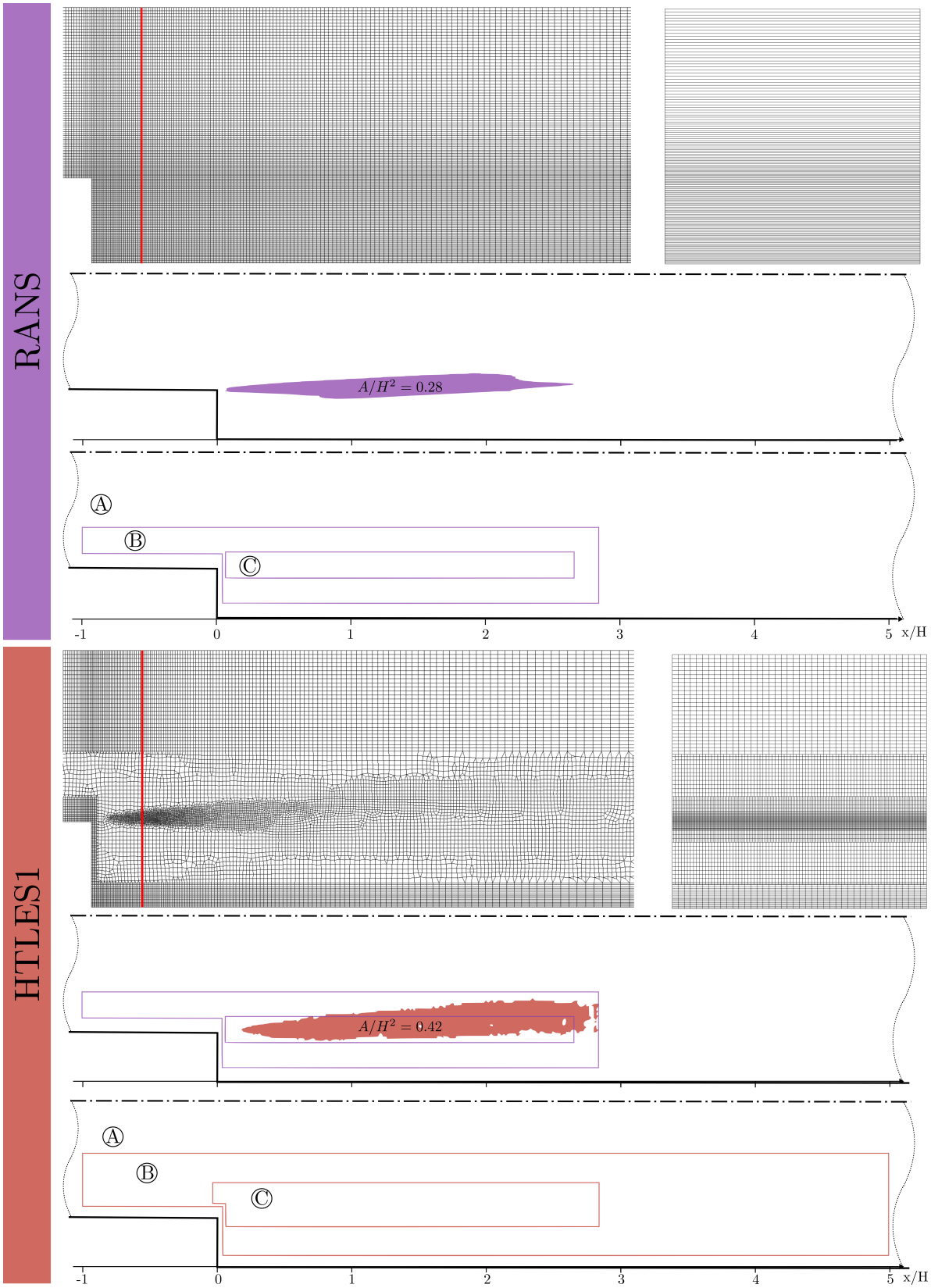

Figure 7: Visualization of the mesh, the regions where $P/\epsilon > \alpha$ and the bounding boxes, for the RANS and HTLES1 computations. Zones A, B, and C correspond to the RANS, transition, and LES zones, respectively. The red line on the mesh view corresponds to the plane $x/H = 0.2$. On the right side, the mesh in this plane is displayed. The values of A/H^2 indicated are the non-dimensional area of the region identified by the criterion.

results of HTLES4 computation are not shown since they are virtually superimposed with those of HTLES3.

In Fig. 10, the target energy ratio (i.e., used in the model, given by Eq. (15)), the effective energy ratio (i.e., computed during the simulation), the streamwise velocity, and the turbulent kinetic energy profiles are plotted. Since the DNS and RANS energy ratios are zero and one, respectively, throughout the entire domain, they are not shown. The HTLES energy ratio profiles depict the interface between RANS and LES regions. The area of the LES region significantly increases from HTLES1 to HTLES2, then stabilizes, reflecting the convergence of the self-adaptive method. The effective energy ratio profiles (Fig. 10b) globally follow those of the energy ratio even if some discrepancies appear, reflecting the fact that the partition of energy approximately reaches the expected level. The results indicate that downstream of the LES region, some resolved scales remain. Mehta et al. [16] made the same observation for the case of a periodic hill, and concluded that it was not a problem, since their results are actually better than pure RANS results. Note that close to the wall, the effective energy ratio is not relevant since both k_m and k_r go to zero. The spikes in the profiles are due to the sharp variations of the total turbulent kinetic energy (Fig. 10d).

Regarding the streamwise velocity (Fig. 10c), upstream the transition region, the RANS mode is imposed and periodic RANS solution imposed at the inlet is preserved. The mesh refinement from $r = 0.15$ (HTLES1) to $r = 0.10$ (others) in the LES region and the definition of the zones has little influence on the streamwise velocity and turbulent kinetic energy (Fig. 10d) profiles, which highlights the robustness of the method. The expansion of the LES zone in the recovery region (HTLES2 and HTLES3) improves the turbulent kinetic energy profiles at $x/H = 3$ and, for HTLES2, which has the largest LES zone, until $x/H = 4$. The spikes of turbulent kinetic energy, principally observed at $x/H = 0$, are due to the rapid RANS/LES transition in the vertical direction and to the forcing term that depends on the variations of the energy ratio. The overshoot of turbulent kinetic energy observed near the step in all HTLES rapidly fades out. A similar behaviour was observed by Mehta et al. [16] for periodic hills and channel flows. Comparing RANS with HTLES3, it appears that RANS significantly underestimates the amount of turbulent kinetic energy from $x/H = 0$ to $x/H = 2$, while it is well estimated by the HTLES3. A close agreement with DNS is found between $x/H = 1$ and $x/H = 3$, which makes possible an accurate prediction of the streamwise velocity profiles between $x/H = 2$ and $x/H = 4$. Downstream of the location $x/H = 4$, the HTLES streamwise velocity profiles are slightly improved when compared to the RANS profiles.

The total Reynolds stresses, $\tau'_{ij} = (\overline{u_i u_j} - \overline{u}_i \overline{u}_j) + \tau^{\mathrm{m}}_{ij}$, and the corresponding anisotropy components, defined as

$$b_{ij} = \frac{\tau'_{ij}}{2k} - \frac{1}{3}\delta_{ij}, \tag{28}$$

are shown in Fig. 11 for HTLES3, at the streamwise locations $x/H = 0$ (top) and $x/H = 1.5$ (bottom). Figs. 11a and 11b show that the fluctuations generated by the forcing do not exhibit the correct anisotropy upstream of the step. This is explained because the volumic forcing acts as an amplifier of the preexisting fluctuations based on Eq. (26), in which τ^{m}_{ij} is the anisotropy tensor given by the linear eddy viscosity models. Correct anisotropy could only be obtained if the RANS model itself was capable of representing it, as with a Reynolds-stress model or an explicit algebraic stress model. However, at $x/H = 1.5$, the Reynolds stresses is quite well predicted, specifically for the τ'_{11} and τ'_{12} components. In Fig. 11d, despite the poor prediction of the anisotropy in $x/H = 0$, the results observed in the LES region are remarkably close to those of the DNS.

The skin friction distribution on the lower wall, shown in Fig. 12, highlights the benefits associated with the self-adaptive method. Indeed, the HTLES3 profile leads to a relatively correct prediction of the negative peak of C_f and gives a very accurate estimate of the reattachment location. Note that the results of HTLES1, which mesh is significantly coarser than that of HTLES3 in the transition and LES regions (see Figs. 7 and 8), are quite accurate, underlying the robustness of the HTLES to mesh coarsening. HTLES gives remarkably better results than RANS in the recirculation zone and downstream of it. Moreover, the peak of C_f observed in DNS at $x/H \approx 0.1$, associated with the secondary counterclockwise recirculation zone, is well reproduced by HTLES while it is not predicted by RANS. Far in the recovery region, HTLES tends toward RANS profiles since the RANS mode is reactivated.

Mean streamlines computed using the line integral convolution (LIC) are displayed in Fig. 13. The two classically observed recirculation zones [6] are visible. The main recirculation zone (clockwise) extends up to $x/H = 2.1$ and the secondary recirculation zone (counterclockwise) to $x/H = 0.4$, to be compared to the DNS values, $x/H = 2.13$ and $x/H = 0.63$, respectively.

The PSD are computed from instantaneous velocity saved every time step, $\mathrm{d}t = 0.0012$ second, during 165 seconds of simulations, resulting in 137 500 instants. For each streamwise location, monitoring points are saved at nine evenly spaced locations in the periodic direction. The data are concatenated leading to a sample size of $N = 1\,237\,500$ velocities for each PSD. The results are smoothed to improve the readability of the figures. The power spectral densities are defined by

$$\int_0^{+\infty} E(\omega)\mathrm{d}\omega = k. \tag{29}$$

In Fig. 14, the PSD reflect the influence of the forcing on the flow, aiming to rapidly develop turbulence structures to compensate for the decrease of the modeled turbulent energy. The peaks observed for $\omega > 3$ Hz highlight the effect of the forcing on the relatively high-frequency structures while the range corresponding to $\omega < 3$ Hz is not affected. Note that a Strouhal number of 0.1 is found which is in agreement with the study of Celenligil and Mellor [3]. The inertial range is scaled with the classical $-5/3$ slope. Because of its lower energy ratio, the probe located at $x/H = 0$ shows a higher

amplitude of the PSD and the sharp decay of the spectrum occurs for higher frequencies than that of $x/H = -0.5$.

The PSD computed downstream of the step are plotted in Fig. 15. In the region of the downstream sensors, the forcing is virtually null since the variations of the energy ratio are low. Hence, contrary the probes located in the forcing region, the PSD decrease monotonously from the inertial to the dissipation ranges. The closer to the wall, the lower the amplitude of the spectra, which is in agreement with the total turbulent kinetic energy profiles. In the inertial range, the $-5/3$ slope is well reproduced for the three y^+ locations. In the high-frequency region, the dissipation scale plays a major role, inducing a fast decay of the turbulent spectrum. The sharp decreases of the slope for very high frequency should not be analyzed since it is beyond the cutoff frequency (colored in light gray). Overall, the PSD express the physical consistency of the turbulent structures generated in the LES region. At $x/H = 4$, the RANS mode is activated and the resolved energy is reduced. The turbulent structures are thus partially filtered out which explains the lower PSD amplitude and the sharper slope in the decay region when compared to the other locations.

The Q-isosurfaces presented in Fig. 16 for HTLES3 show that the active HTLES rapidly develops resolved scales, thanks to the volume forcing. Indeed, turbulent structures are remarkably observed right from the beginning of the LES region. However, downstream of the LES region, the structures are advected into the RANS zone and are only gradually dissipated by the RANS eddy viscosity. As can be seen in Fig. 12, the solution transitions in this region from a LES to a RANS behavior.

5. Conclusions and future work

In this paper, a self-adaptive strategy is proposed to mitigate the influence of the user on the results of hybrid RANS/LES computations. To avoid the definition of the RANS and LES zones by the user choices made at the time of the construction of the mesh, the zones where to switch to LES are determined by physical criteria, and the mesh is also refined in this zone to target a resolution obtained based on a physical criterion. The method is assessed on a backward-facing step with the HTLES-$k-\omega$-SST model.

Several possible physical criteria within the context of self-adaptive hybrid RANS/LES are investigated and the P/ϵ criterion, which assesses the turbulence equilibrium, is selected. Starting from a RANS computation for initialization, successive HTLES are carried out using the results of the previous computation to generate the mesh of the next simulation.

The outcomes of the study show that the self-adaptive strategy converges in four iterations. The statistically-averaged profiles and the friction coefficient are significantly improved when compared to the RANS computation and are in good agreement with the reference DNS results. The assessment of the components of the Reynolds stress anisotropy tensor emphasizes the reliability of the active HTLES and its benefits when associated with the proposed adaptive approach. The combination of the quite accurate prediction of the turbulent kinetic energy, the reliable estimate of the turbulence anisotropy, and the conformity of the spectra expresses the physical consistency of the turbulent structures generated. Downstream of the LES region, the turbulent structures are only gradually dissipated by the RANS eddy viscosity as observed on the Q-isosurfaces and power spectral densities.

Although many parameters can be adjusted and/or generalized, this study demonstrates that a self-adaptive strategy can be used effectively. As the algorithm is initialized from a RANS calculation, the user's influence on the results is reduced to the same level as for a RANS calculation. The user's subjective choices, based on his intuition and a priori knowledge of the flow physics, may lead to very different zones being defined depending on the user, as illustrated in Fig. 1. Obviously, the criteria used in the self-adaptive algorithm have a definite influence on the results, but if these criteria are fixed once and for all, the results are reproducible and independent of the user, which is of great importance for industrial applications.

Since the method has been developed validated on a specific flow, future work must be devoted to the application of the self-adaptive strategy to other test cases, possibly with the application of additional physical criteria, intending to develop a robust methodology useful for a wide range of applications.

Acknowledgments

This study was funded by E2S UPPA (ANR-16-IDEX-0002) and INRIA in the framework of the ASTURIES project (grant E2S-20-ScientificChallenges-01). The computing resources were provided by MCIA (Mésocentre de Calcul Intensif Aquitain) and GENCI-IDRIS (Grants 2022-A0122A10980 and 2023-A0142A10980).

CRediT authorship contribution statement

Martin David: Methodology; Software; Investigation; Visualization; Writing/Original Draft Preparation. **Mahitosh Mehta:** Investigation; Visualization; Reviewing. **Rémi Manceau:** Conceptualization; Methodology; Supervision; Writing/Review & Editing; Funding Acquisition; Project Administration.

References

[1] Archambeau, F., Méchitoua, N., Sakiz, M., 2004. Code Saturne: A Finite Volume Code for the computation of turbulent incompressible flows - Industrial Applications. International Journal on Finite Volumes 1, http://www.latp.univ.

[2] Baglietto, E., Lenci, G., Concu, D., 2017. STRUCT: A Second-Generation URANS Approach for Effective Design of Advanced Systems, in: ASME 2017 Fluids Engineering Division Summer Meeting, American Society of Mechanical Engineers Digital Collection.

[3] Celenligil, M.C., Mellor, G.L., 1985. Numerical Solution of Two-Dimensional Turbulent Separated Flows Using a Reynolds Stress Closure Model. Journal of Fluids Engineering 107, 467–476.

[4] Chaouat, B., 2017. The State of the Art of Hybrid RANS/LES Modeling for the Simulation of Turbulent Flows. Flow, Turbulence and Combustion 99, 279–327.

[5] Chaouat, B., Schiestel, R., 2005. A new partially integrated transport model for subgrid-scale stresses and dissipation rate for turbulent developing flows. Physics of Fluids 17, 1–19.

[6] Chen, L., Asai, K., Nonomura, T., Xi, G., Liu, T., 2018. A review of Backward-Facing Step (BFS) flow mechanisms, heat transfer and control. Thermal Science and Engineering Progress 6, 194–216.

[7] Duffal, V., de Meux, B.d.L., Manceau, R., 2022. Development and Validation of a new formulation of Hybrid Temporal Large Eddy Simulation. Flow, Turbulence and Combustion 108, 42.

[8] Fadai-Ghotbi, A., Friess, C., Manceau, R., Gatski, T.B., Borée, J., 2010. Temporal filtering: A consistent formalism for seamless hybrid RANS–LES modeling in inhomogeneous turbulence. International Journal of Heat and Fluid Flow 31, 378–389.

[9] Fröhlich, J., von Terzi, D., 2008. Hybrid LES/RANS methods for the simulation of turbulent flows. Progress in Aerospace Sciences 44, 349–377.

[10] Geuzaine, C., Remacle, J.F., 2009. Gmsh: A 3-D finite element mesh generator with built-in pre- and post-processing facilities. International Journal for Numerical Methods in Engineering 79, 1309–1331.

[11] Girimaji, S.S., 2005. Partially-Averaged Navier-Stokes Model for Turbulence: A Reynolds-Averaged Navier-Stokes to Direct Numerical Simulation Bridging Method. Journal of Applied Mechanics 73, 413–421.

[12] Heinz, S., Mokhtarpoor, R., Stoellinger, M.K., 2020. Hybrid RANS-LES Methods with Continuous Mode Variation, in: García-Villalba, M., Kuerten, H., Salvetti, M.V. (Eds.), Direct and Large Eddy Simulation XII, Springer International Publishing, Cham. pp. 441–447.

[13] Krumbein, B., Maduta, R., Jakirlić, S., Tropea, C., 2020. A Scale-Resolving Elliptic-Relaxation-Based Eddy-Viscosity Model: Development and Validation, in: Dillmann, A., Heller, G., Krämer, E., Wagner, C., Tropea, C., Jakirlić, S. (Eds.), New Results in Numerical and Experimental Fluid Mechanics XII, Springer International Publishing, Cham. pp. 90–100.

[14] Lamballais, E., 2014. Direct numerical simulation of a turbulent flow in a rotating channel with a sudden expansion. Journal of Fluid Mechanics 745, 92–131.

[15] Limare, A., Borouchaki, H., Brenner, P., 2020. Adaptive Mesh Refinement with an Automatic Hybrid RANS/LES Strategy and Overset Grids, in: Hoarau, Y., Peng, S.H., Schwamborn, D., Revell, A., Mockett, C. (Eds.), Progress in Hybrid RANS-LES Modelling, Springer International Publishing, Cham. pp. 159–168.

[16] Mehta, M., Manceau, R., Duffal, V., de Laage de Meux, B., 2023. An active hybrid Reynolds-averaged Navier–Stokes/large eddy simulation approach for gray area mitigation. Physics of Fluids 35, 125116.

[17] Menter, F., Egorov, Y., 2010. The Scale-Adaptive Simulation Method for Unsteady Turbulent Flow Predictions. Part 1: Theory and Model Description. Flow Turbulence and Combustion 85, 113–138.

[18] Menter, F.R., 1994. Two-equation eddy-viscosity turbulence models for engineering applications. AIAA Journal 32, 1598–1605.

[19] Park, M.A., Loseille, A., Krakos, J., Michal, T.R., Alonso, J.J., 2016. Unstructured Grid Adaptation: Status, Potential Impacts, and Recommended Investments Towards CFD 2030, in: 46th AIAA Fluid Dynamics Conference, American Institute of Aeronautics and Astronautics, Washington, D.C.

[20] Perot, J.B., Gadebusch, J., 2007. A self-adapting turbulence model for flow simulation at any mesh resolution. Physics of Fluids 19, 115105.

[21] Perot, J.B., Gadebusch, J., 2009. A stress transport equation model for simulating turbulence at any mesh resolution. Theoretical and Computational Fluid Dynamics 23, 271–286.

[22] Pope, S.B., 2004. Ten questions concerning the large-eddy simulation of turbulent flows. New Journal of Physics 6, 35.

[23] Reuß, S., Knopp, T., Probst, A., Orlt, M., 2015. Assessment of Local LES-Resolution Sensors for Hybrid RANS/LES Simulations, in: Girimaji, S., Haase, W., Peng, S.H., Schwamborn, D. (Eds.), Progress in Hybrid RANS-LES Modelling, Springer International Publishing, Cham. pp. 93–103.

[24] Spalart, P.R., 2000. Strategies for turbulence modelling and simulations. International Journal of Heat and Fluid Flow 21, 252–263.

[25] Spalart, P.R., Venkatakrishnan, V., 2016. On the role and challenges of CFD in the aerospace industry. The Aeronautical Journal 120, 209–232.

[26] Tennekes, H., 1975. Eulerian and Lagrangian time microscales in isotropic turbulence. Journal of Fluid Mechanics 67, 561–567.

[27] Woodruff, S., 2019. Adaptive Embedded LES of the NASA Hump, in: AIAA Scitech 2019 Forum. American Institute of Aeronautics and Astronautics. AIAA SciTech Forum.

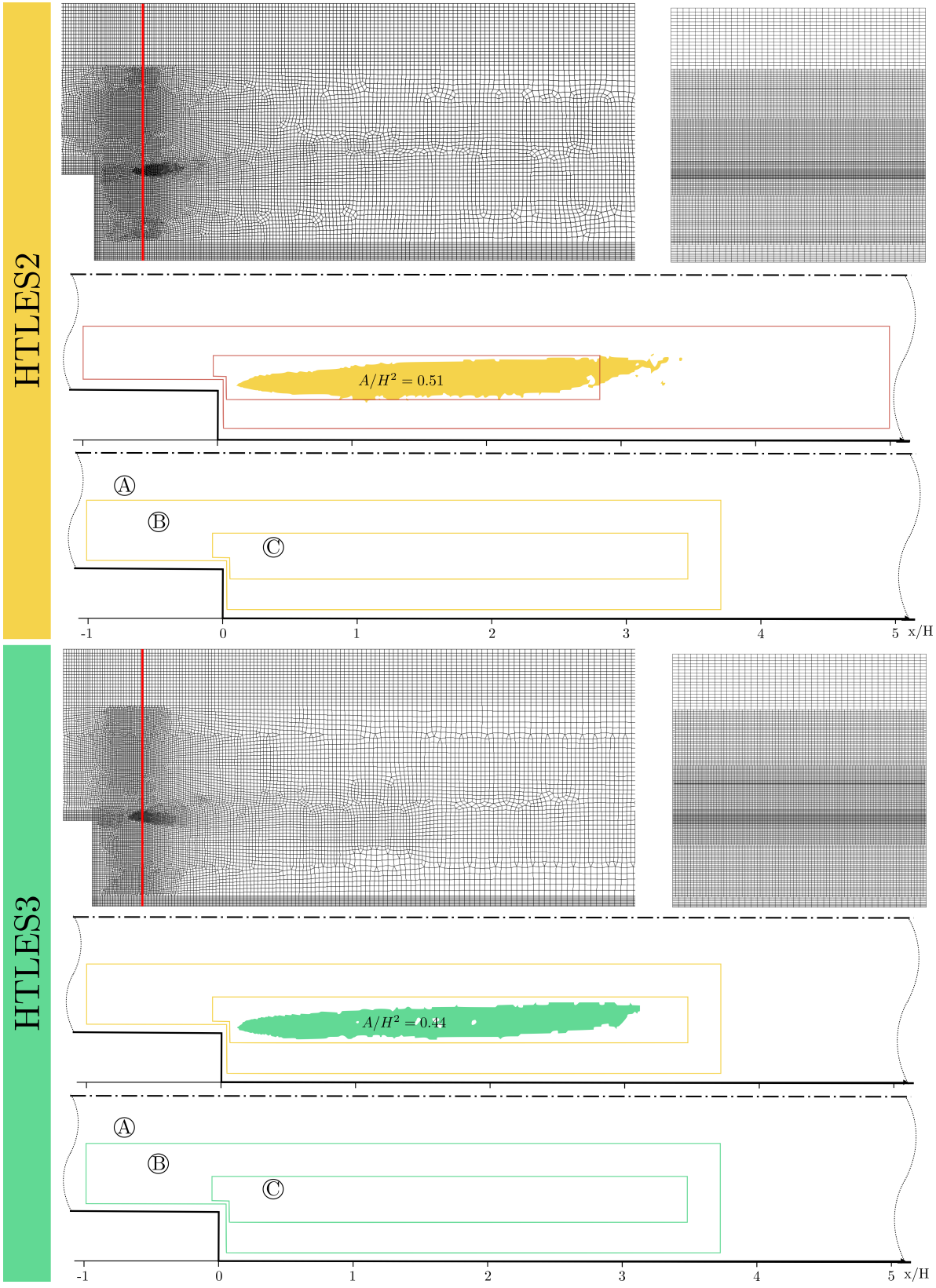

Figure 8: Same as Fig. 7 for HTLES2 and HTLES3.

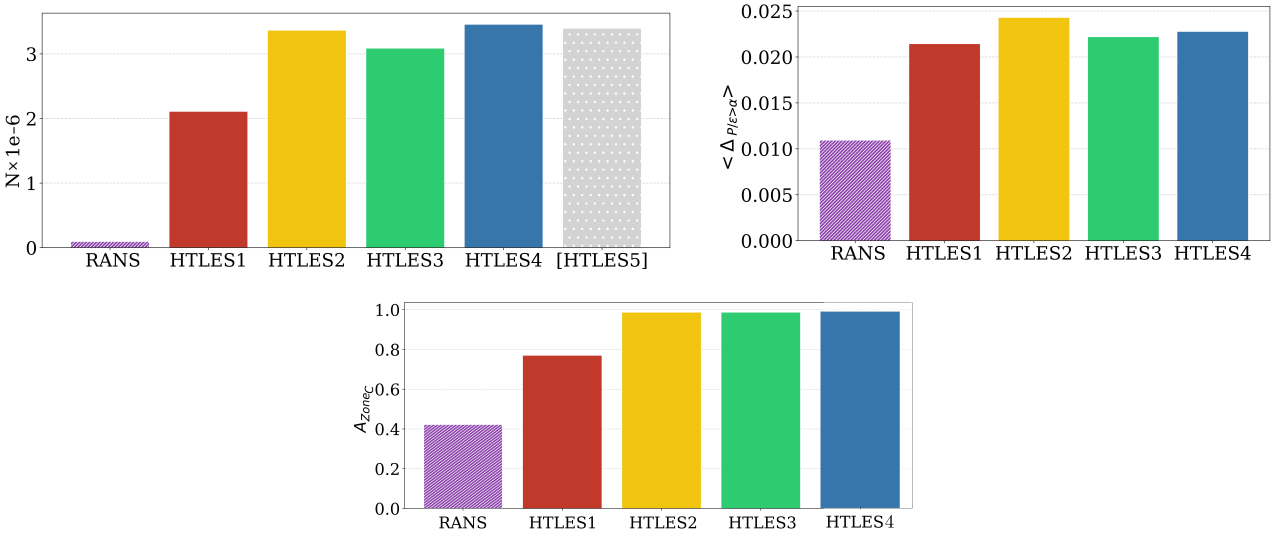

Figure 9: Top: number of cells and averaged value of Δ in the region where $P/\epsilon > \alpha$. Bottom: area of Zone C. Note that HTLES5 has not been run, but the mesh, built with the results of HTLES4, is displayed to highlight the convergence of the algorithm.

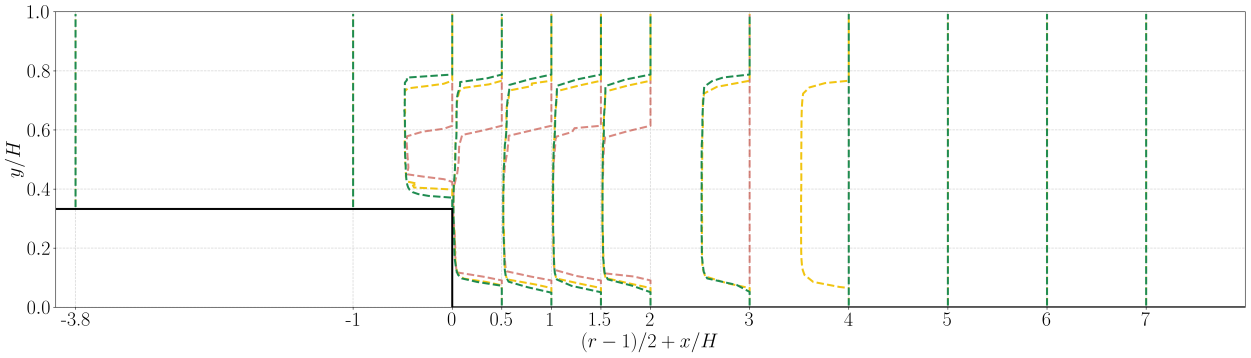

(a) Energy ratio

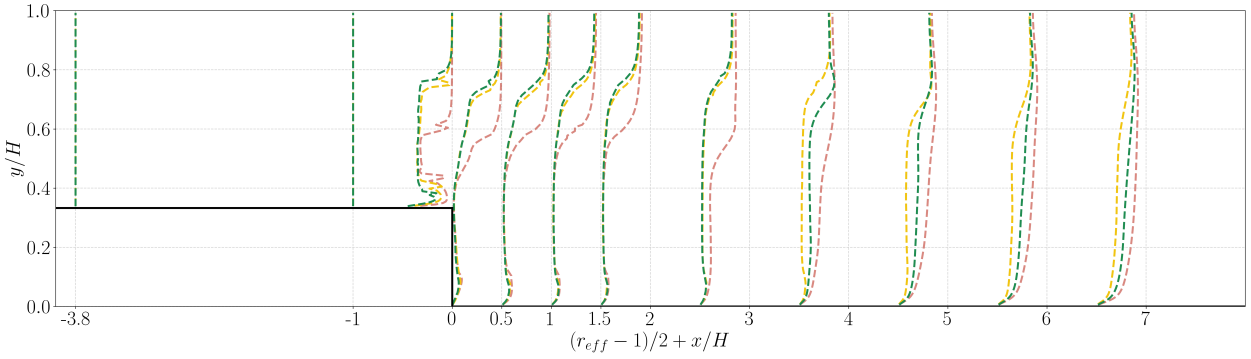

(b) Effective energy ratio

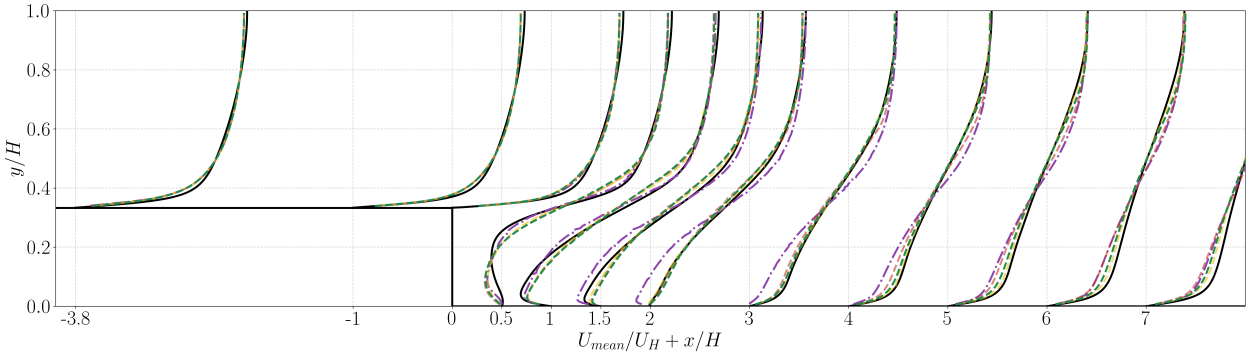

(c) Streamwise velocity

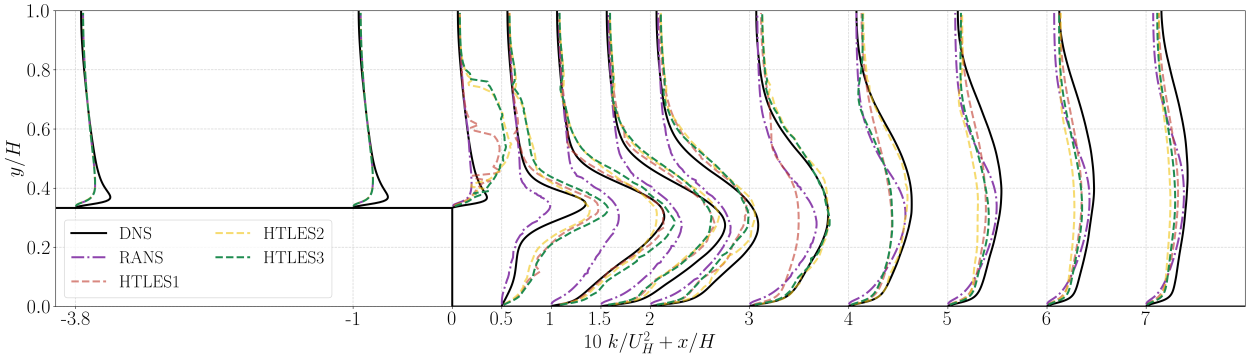

(d) Total turbulent kinetic energy

Figure 10: Profiles in the y direction for 12 streamwise locations. DNS results are from Lamballais [14].

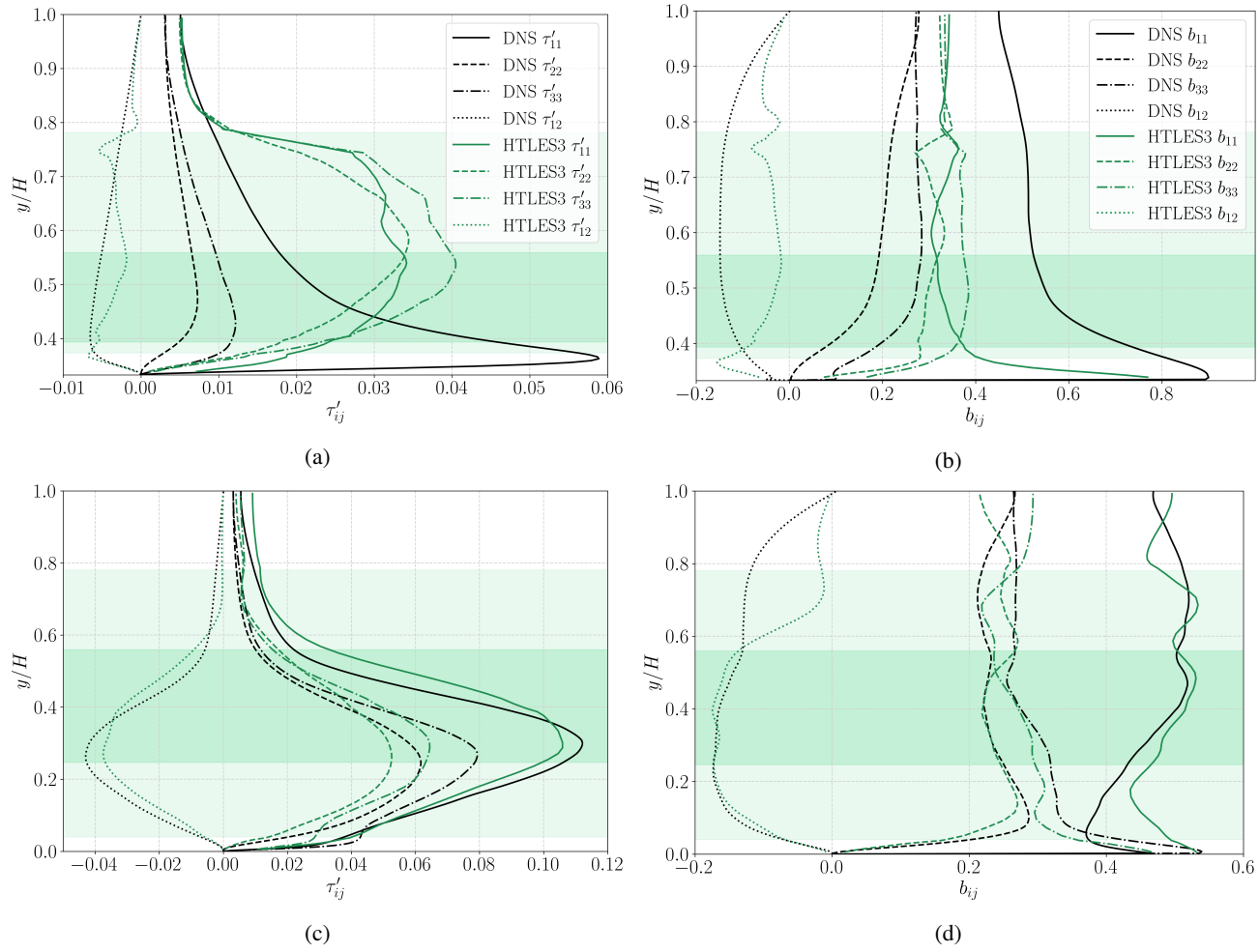

Figure 11: Profiles of the Reynolds stresses (left) and anisotropy components (right) in the y direction for $x/H = 0$ (top) and $x/H = 1.5$ (bottom). The white, light green and medium green zones show the RANS, transition, and LES zones, respectively. DNS results are from Lamballais [14].

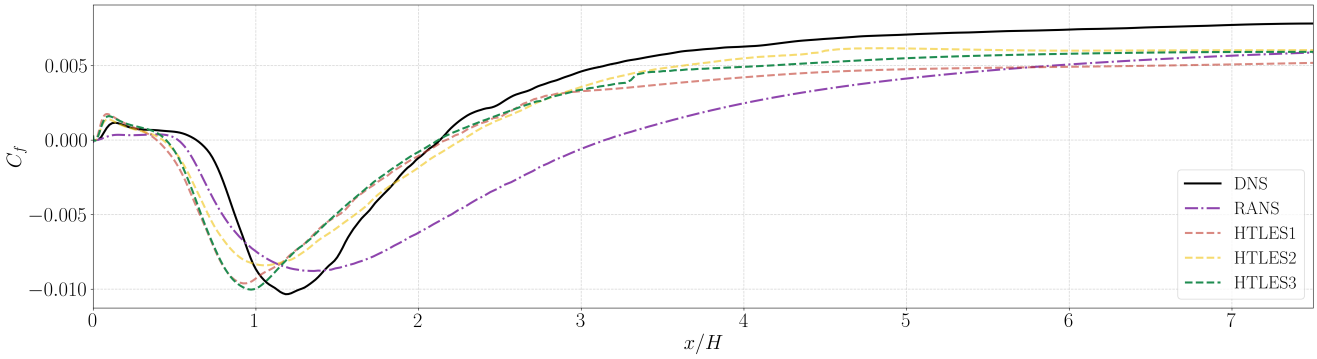

Figure 12: Distribution of skin friction on the wall downstream of the step. DNS results are from Lamballais [14].

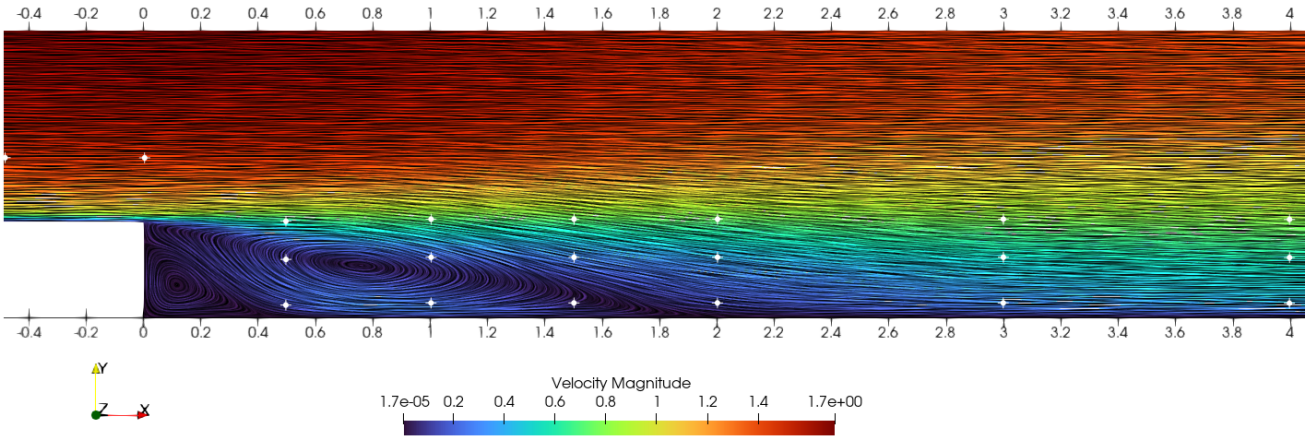

Figure 13: Mean streamlines of the HTLES3 colored with velocity magnitude.

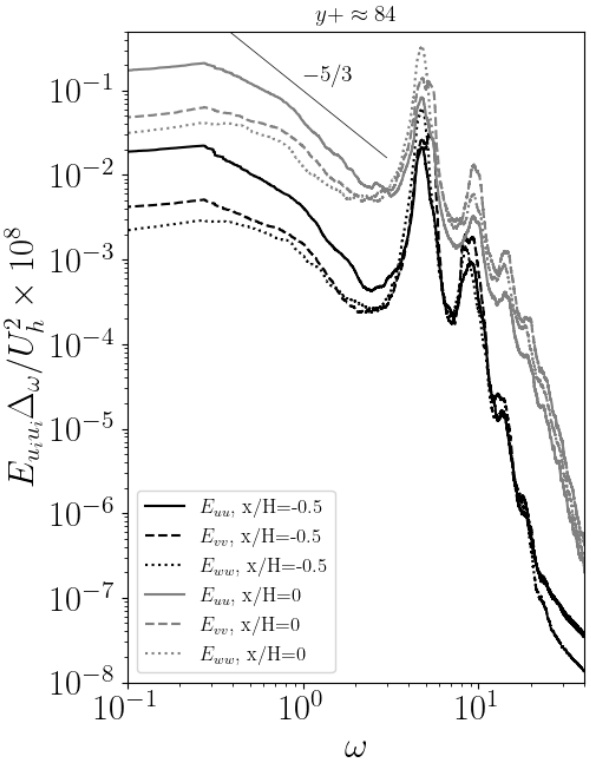

Figure 14: Power spectral densities of the streamwise, wall-normal, and spanwise velocities obtained with HTLES3, upstream of the step, at $y/H = 0.557$ (corresponding to $y^+ \approx 84$). The results are normalized with the velocity, $U_h = 3U_H/2$, and the frequency step, Δ_ω. The cutoff frequency, $\omega_c = 50$ Hz, is higher than the maximum plotted frequency.

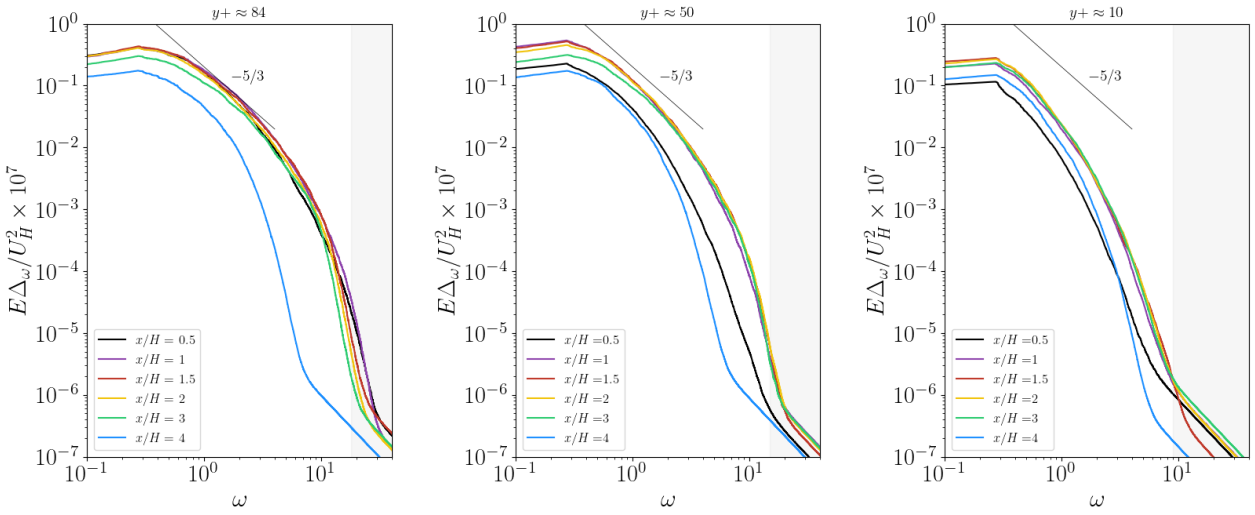

Figure 15: Power spectral densities obtained with HTLES3 for $y/H = 1/3$, $y/H = 0.2$, and $y/H = 0.04$ (corresponding to $y^+ \approx 84$, $y^+ \approx 50$, and $y^+ \approx 10$, respectively), from left to right. The results are normalized with the velocity, U_H, and the frequency step, Δ_ω. The ranges in light gray color show frequencies higher than the cutoff frequency.

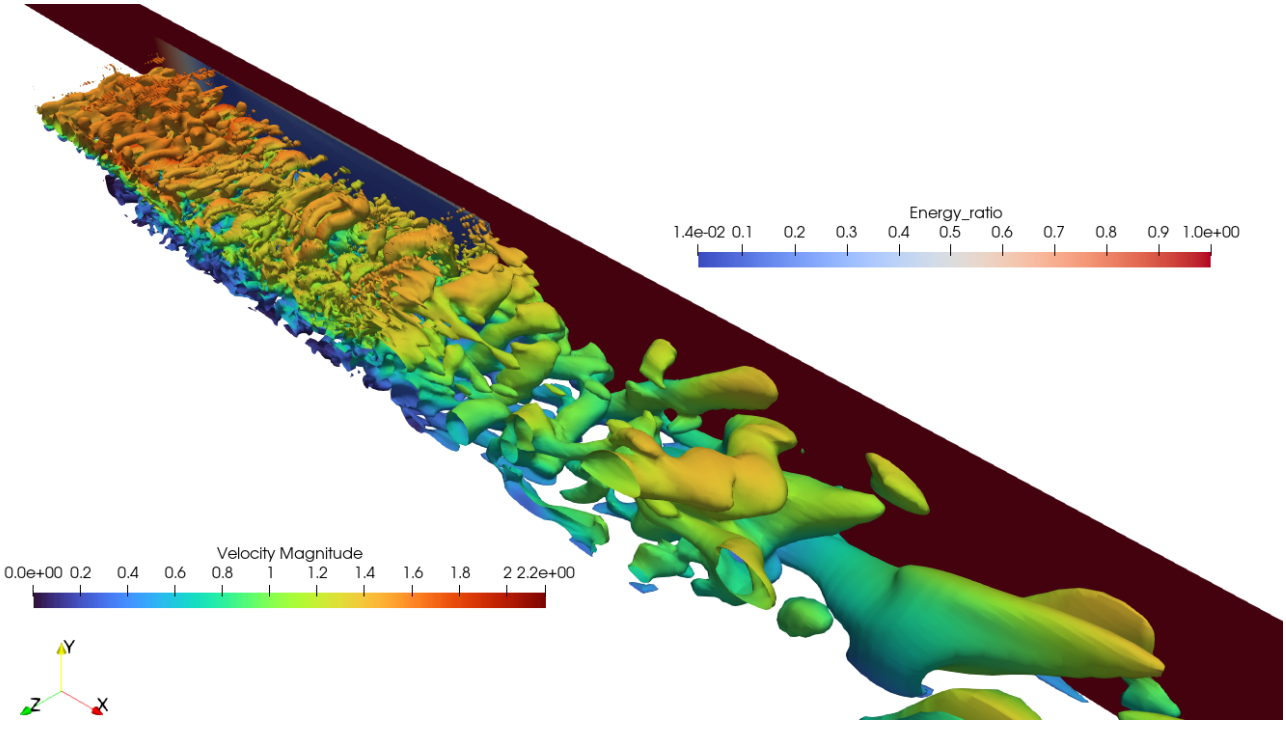

Figure 16: Q-isosurfaces colored by the velocity magnitude ($Q = 0.5U_H^2/H^2$) and targeted turbulent energy ratio for the HTLES3.